Thioester synthesis by geoelectrochemical CO_2 fixation on Ni sulfides

Norio Kitadai[1,2]*, Ryuhei Nakamura[2,3], Masahiro Yamamoto[1], Satoshi Okada[4], Wataru Takahagi[1,5], Yuko Nakano[2], Yoshio Takahashi[6], Ken Takai[1], Yoshi Oono[7]

Thioester synthesis via CO_2 fixation by CO dehydrogenase/acetyl-CoA synthase is among the most ancient autotrophic metabolism often suggested to have a prebiotic root. Here we demonstrate that, under an electrochemical condition realizable in early ocean hydrothermal systems, nickel sulfide (NiS) gradually reduces to Ni^0, thereby drastically enhancing its capability of driving nonenzymatic CO_2 fixation. It catalyzes CO_2 electroreduction to CO, concentrates CO on the surface Ni^0 sites, and promotes CO condensation to a thioester in the presence of methanethiol. Even greater CO-to-thioester reaction efficiency is realized with NiS coprecipitating with FeS or CoS. Considering the central role of Ni in the enzymatic process mentioned above, our demonstrated thioester synthesis by the partially electroreduced NiS could have a direct implication to the autotrophic origin of life.

Thioester synthesis via acetylation of coenzyme A is a universal metabolic strategy of energy and carbon conservation. Molecular phylogenetics suggests that this biological reaction already functioned in the last universal common ancestor with carbon monoxide dehydrogenase (CODH) and acetyl-CoA synthase (ACS) as the prime catalysts. (*1*). At the Ni-based active centers bridged to an (or multiple) Fe−S cluster(s), CODH reduces CO_2 to CO using electrons typically taken from hydrogen (H_2), whereas ACS condenses CO with CoA and the methyl group to form acetyl-CoA. These enzymatic processes often remind us of their prebiotic origins in a hydrothermal vent environment rich in CO_2, H_2, and (Fe,Ni)S minerals on the Hadean ocean floor (*2*,*3*).

However, nonenzymatic realization of the two reaction steps remains a great experimental challenge. The CO_2-to-CO reduction requires a highly reducing potential that is inaccessible by the H^+/H_2 redox couple in the absence of flavin-based electron bifurcation (*4*) (fig. S1). In the ACS catalytic cycle, the active Ni site serves as both the electron donor and accepter through changing its oxidation state between +1 and +3, facilitating both the reduction and oxidation intermediate steps (*5*). Such valence change of Ni has never been observed in natural Ni-bearing minerals. Although Huber and Wächtershäuser (*6*) demonstrated S-methyl thioacetate (MTA) synthesis from CO and methanethiol in the presence of NiS as a potential prebiotic precursor of the ACS reaction, the yield was very low (0.2% based on the initial amount of CO) even under the optimum condition (pH 1.6 and 100°C) that is uncommon in nature.

How were these difficulties in CO_2-to-CO reduction and CO condensation overcome in early ocean hydrothermal systems? A clue is an *on-site* observation by Yamamoto et al. (*7*) of electricity generation in deep-sea hydrothermal vent chimneys and mineral deposits. The geoelectricity arises from the redox coupling between hydrothermal fluid chemicals and seawater-dissolved species via electrically conducting yet thermally insulating sulfide rocks (fig. S1) (*8*). Considering cool (0–50 °C) and slightly acidic (pH 6–7) character of the ancient seawater (*9*), together with pH and temperature dependences of the H^+/H_2 and CO_2/CO redox potentials (*10*,*11*) (fig. S1), H_2-rich alkaline hydrothermal systems must have readily provided negative electric potentials favorable for the CO_2-to-CO conversion at the chimney-ancient seawater interface. We previously demonstrated efficient CO_2 electroreduction to CO on some metal sulfide catalysts (for example, cadmium sulfide) under a simulated early ocean geoelectrochemical condition (*12*).

[1]Super-cutting-edge Grand and Advanced Research (SUGAR) Program, Institute for Extra-cutting-edge Science and Technology Avant-garde Research (X-star), Japan Agency for Marine-Earth Science and Technology (JAMSTEC), 2-15 Natsushima-cho, Yokosuka 237-0061, Japan.
[2]Earth-Life Science Institute, Tokyo Institute of Technology, 2-12-1 Ookayama, Meguroku, Tokyo 152-8550, Japan.
[3]Biofunctional Catalyst Research Team, RIKEN Center for Sustainable Resource Science, 2-1 Hirosawa, Wako, Saitama 351-0198, Japan.
[4]Research Center for Bioscience and Nanoscience (CeBN), Research Institute for Marine Resources Utilization, Japan Agency for Marine-Earth Science and Technology (JAMSTEC), 2-15 Natsushima-cho, Yokosuka 237-0061, Japan.
[5]Department of Chemistry, Graduate School of Science, The University of Tokyo, 7-3-1 Hongo, Bunkyo-ku, Tokyo 113-0033, Japan.
[6]Department of Earth and Planetary Science, Graduate School of Science, The University of Tokyo, 7-3-1 Hongo, Bunkyo-ku, Tokyo 113-0033, Japan.
[7]Department of Physics, University of Illinois at Urbana-Champaign, 1110W. Green Street, Urbana, IL 61801-3080, USA (retired).
*Correspondence to: nkitadai@jamstec.go.jp

It was also found that FeS undergoes day-scale electroreduction to Fe^0 (*13*). The resultant FeS-Fe^0 assemblage, named FeS_PERM (FeS partially electroreduced to metal), showed exceptional capability of promoting various prebiotically important reactions owing to synergy between surface Fe sites with different oxidation states (Fe^{2+} and Fe^0) (*14,15*). In our previous works, NiS exhibited neither CO evolution nor the Ni^0 formation detectable by X-ray diffraction (XRD) analysis.

Our further investigation presented below, however, found non-crystalline growth of Ni^0 under geochemically feasible potential conditions. The NiS_PERM formed under CO_2 atmosphere retains a substantial amount of CO produced and bound on the surface Ni^0 sites. In the presence of methanethiol as the source of the methyl group (*6*), the surface-bound CO highly efficiently converts to a thioester (MTA) even at room temperature and neutral pH. Notice that the surface-bound CO that forms during CO_2 electroreduction is generally recognized as a poison of surface electrocatalytic activity (*16,17*), but here we use it as a key component of thioester. Considering the significance of thioesters in biosynthesis and also in organic chemical synthesis (*18*), our demonstrated CO_2 fixation pathway must be meaningful not only for understanding the origin of life but also for engineering CO_2 utilization scheme.

We prepared metal sulfides including NiS by simply mixing an aqueous solution of the corresponding metal chloride and an aqueous solution of sodium sulfide. The obtained sulfides were exposed to a constant electric potential for 7 days in 100 mM NaCl at room temperature (25 ± 2°C) under continuous CO_2 bubbling that maintained the solution pH at 6 ± 0.25 (figs. S2 and S3). The electrolyzed sulfides were then separated from the supernatant solution, dried under vacuum, and used for the following experiments.

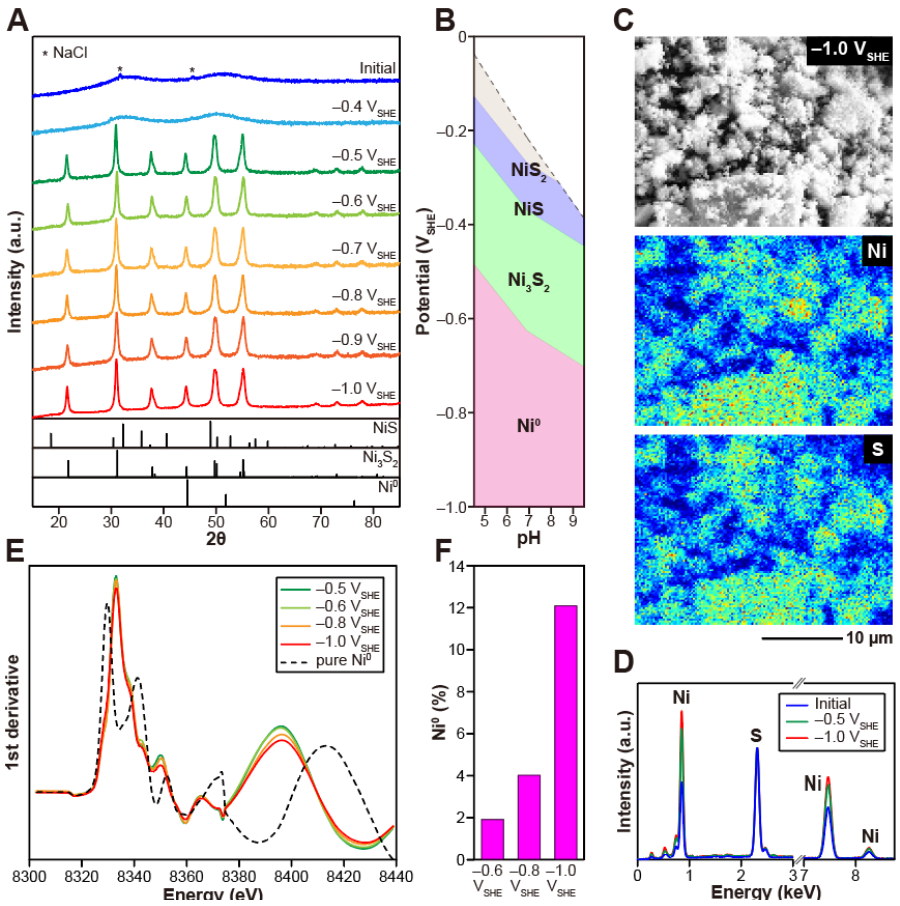

Fig. 1. NiS electroreduction results characterized by (A) XRD patterns, (B) thermodynamic calculation, (C, D) SEM-EDX mapping data, and (E, F) nickel K-edge XANES spectra. (C) presents the EDX mapping data for the NiS electrolyzed at –1.0 V_{SHE}. In **(D)**, the S signal intensities (2.3 keV) of three different spectra are matched with each other for comparison. **(E)** The first derivative XANES spectra is shown.

The NiS consists of aggregated nanoparticles with an average particle diameter of 15 ± 11 nm (fig. S6). Although no significant morphological change was caused (fig. S6), exposure at –0.5 V_{SHE} (volt versus the standard hydrogen electrode) led to the desulfurization of NiS to heazlewoodite (Ni_3S_2) (Fig. 1A), consistent with thermodynamic calculation (Fig. 1B). Further reduction of Ni_3S_2 at lower electric potentials was indicated by energy dispersive X-ray spectroscopy (EDS) mapping on the NiS particles electrolyzed at –1.0 V_{SHE} (Fig. 1C), where a clear decrease in the sulfur signal intensity relative to nickel was observed in comparison with pure NiS, and with the NiS electrolyzed at –0.5 V_{SHE} (Fig. 1D). In agreement with the EDS result, nickel K-edge X-ray absorption near-edge structure (XANES) of the NiS samples showed spectral changes with decreasing potential from –0.5 to –1.0 V_{SHE} (Fig. 1E) attributable to the occurrence and growth of Ni^0 in Ni_3S_2 up to the Ni^0 percentage of 12% at –1.0 V_{SHE} (Fig. 1F and fig. S11). Similarly, XANES analysis allowed us to estimate 7% conversion of CoS to Co^0 at –1.0 V_{SHE} (fig. S12). Thus, NiS_PERM and CoS_PERM are formed at –1.0 V_{SHE} and even less negative potentials near their sulfide/metal equilibria (Fig. 1B and F, fig. S11 and S12) just as in the FeS case. However, in contrast to FeS that exhibited broad but clear XRD signals for Fe^0 even at –0.7 V_{SHE} (fig. S8) (*13*), NiS showed no XRD signal for Ni^0 in the examined potential range (≤–1.0 V_{SHE}) (Fig. 1A). The Ni^0 percentage up to 12% (Fig. 1F) is well above the detection limit of XRD (fig. S10) if the formation of meso- or macroscopic crystalline structure is assumed. Thus, NiS_PERM would be with more finely dispersed zerovalent metal than FeS_PERM.

To explore the possibility of CO production and accumulation on the metal-sulfide PERMs as in the case of several pure metals (*16*,*17*), we prepared metal-sulfide PERMs under CO_2 atmosphere as described above, dissolved the dried solids completely in 35% hydrogen chloride, and quantified the released CO by gas chromatography (fig. S18 and Movie S1). Except for FeS, all the sulfides exposed at ≤–0.6 V_{SHE} were found to retain CO (Fig. 2A and Table S2). The threshold potential is close to the sulfide/metal equilibrium potentials for Ni and Co (–0.57 V_{SHE} for both; Fig. 1B and fig. S4), and is also near the thermodynamic

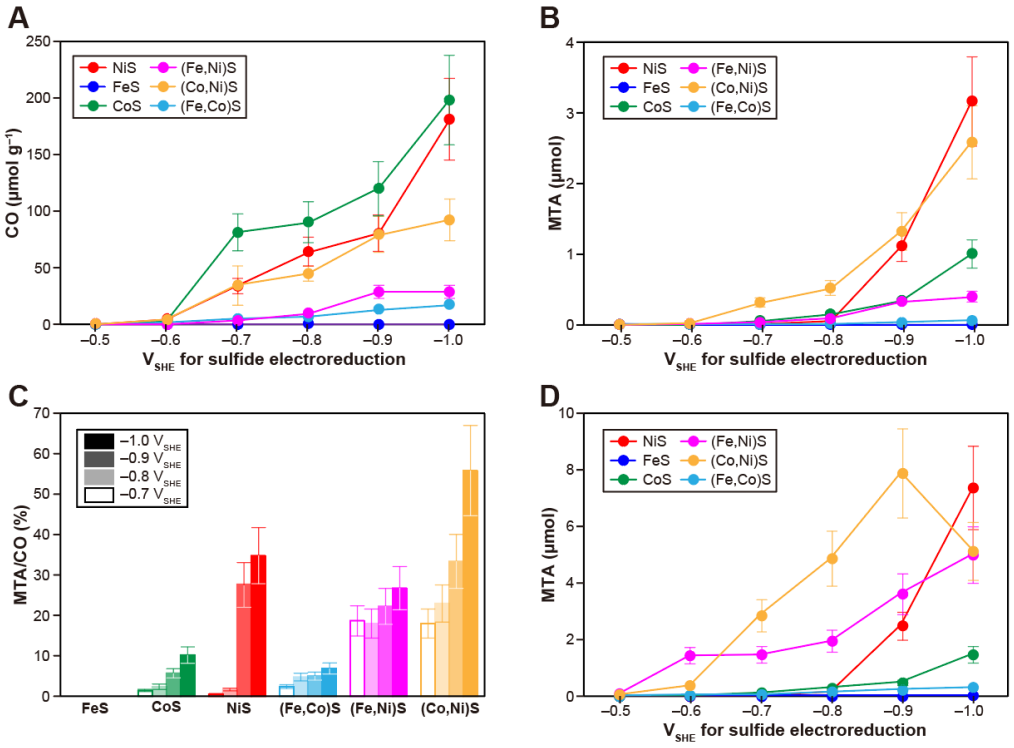

Fig. 2. Nonenzymatic CO_2 electroreduction to CO (A) and CO condensation to S-methyl thioacetate (MTA) (B–D) with the metal-sulfide_PERMs. The surface-bound CO on the electrolyzed sulfides were quantified **(A)** and used as a carbon source for the MTA synthesis in the presence of methanethiol (75 μmol per 50 mg of sulfide) **(B)**. The percentages of CO condensed to form MTA are shown in **(C)**. **(D)** The MTA synthesis were examined with CO and methanethiol externally added (75 μmol for each). The yield of MTA on (Co,Ni)S declined at the lowest potential because of depletion of methanethiol (Table S3).

CO_2/CO redox potential at the condition of sulfide electrolysis (–0.50 V_{SHE}; fig. S1). The amount of CO increased with decreasing the potential, up to 180 ± 40 μmol g^{-1} for the case of NiS. Because sulfurized Ni binds CO considerably more weakly than pure Ni^0 (*19*), the observed CO should mostly derive from the CO produced and accumulated on the surface Ni^0 sites. In fact, the maximum adsorption (180 ± 40 μmol g^{-1}) corresponds to the surface coverage of one CO molecule per 8 ± 3 surface Ni atoms (fig. S13), consistent with the percentage of Ni^0 grown at –1.0 V_{SHE} (Fig. 1F). The similar interpretation should be applicable to the adsorption behavior of CO on the electrolyzed CoS (*20*). Coprecipitation with FeS led to decline of the amounts of CO on NiS and CoS (Fig. 2A) probably because of the decrease in the surface reactive sites.

We mixed the metal-sulfide PERMs retaining the surface-bound CO (Fig. 2A) (50 mg for each) with an aqueous solution of sodium methanethiolate (75 μmol) in a serum bottle (13.8 ml), and agitated at room temperature for up to 7 days. pH was buffered at neutral (7.0 ± 0.5) by filling the gas space with CO_2 (1 atm). Despite this very mild condition, gas chromatograph–mass spectrometry analysis revealed highly efficient MTA formation in the presence of specific electrolyzed sulfides (Fig. 2B and C). Organosulfur compounds detected with the amount higher than 0.01 μmol were methanethiol, MTA, dimethyl sulfide and dimethyl disulfide (figs. S19 and S20), among which MTA was the sole product built from CO and methanethiol

$$CO + 2CH_3SH \rightarrow CH_3COSCH_3 + H_2S \qquad (1)$$

When CO, as well as methanethiol, were initially introduced with equal amounts (75 μmol, or 0.14 bar in the gas space) in the presence of NiS_PERM formed at –1.0 V_{SHE}, the yield of MTA more than doubled, compared with the case without CO in the initial gas phase (3.2 ± 0.6 → 7.4 ± 1.5 μmol; Fig. 2D and fig. S21A). In contrast, under the same initial condition with CO, few or no detectable MTA was formed in the presence of pure NiS, the Ni_3S_2 prepared at –0.5 V_{SHE}, or pure Ni^0 (fig. S21 and Table S4), indicating the necessity of the coexistence of zerovalent and non-zerovalent Ni surface sites for efficient MTA production. It is also notable that the MTA yield decreased steeply as the NiS electroreduction potential was positively changed from –1.0 to –0.8 V_{SHE} (Fig. 2B to D) although –0.8 V_{SHE} is still sufficient for the Ni^0 generation (Fig. 1F). One possible interpretation is that the surface density of Ni^0 is an important factor for the condensation of CO with methanethiol (fig. S26); this process may occur at a surface Ni^0 site with the aid of closely located other Ni^0 atoms and non-zerovalent Ni atoms working as electron donors and acceptors, respectively.

Interestingly, even greater CO-to-MTA reaction efficiencies were obtained with the NiS coprecipitating with FeS or CoS (Fig. 2C). Up to 56 ± 10% of the surface-bound CO, produced by CO_2 reduction, converted to MTA on the electrolyzed (Co,Ni)S. (Fe,Ni)S produced a considerable amount of MTA from initially introduced CO and methanethiol even after the –0.6 V_{SHE} electrolysis (Fig. 2D). Given FeS's electroreduction reactivity higher than that of NiS (figs. S7 and S8), Fe in the electrolyzed (Fe,Ni)S may be expected to assist the Ni's performance as an electron donor at an intermediate reduction step. The Fe's supportive role is also seen in the ACS-reaction as the form of ferredoxin serving as the redox mediator (*5*). The observed selectivity enhancement by Co (Fig. 2C) reminds us of the involvement of Co in the enzymatic process as a transporter of the methyl group (*5*).

Our experiments revealed that partial electroreduction of NiS to Ni^0, that is, the formation of NiS_PERM, markedly enhances NiS's capability of driving thioester synthesis via CO_2-to-CO reduction and CO condensation (Fig. 2). Ancient seawater was rich in Ni^{2+} owing to much greater mantle activity than the present level (*21*). Because Ni^{2+} is almost insoluble in alkaline sulfide condition, Ni-bearing sulfides must have precipitated at the vent-seawater interface in early ocean alkaline hydrothermal systems, and has been exposed to a sustained negative potential by the geoelectrochemical processes (fig. S1). The potential level required for the Ni^0 formation and the surface-catalyzed CO production (≤–0.6 V_{SHE}; Figs. 1 and 2) is attainable under moderately hot, H_2-rich, and alkaline conditions as observed even in the present-day hydrothermal systems (*22*). The surface-bound CO is stable in NaCl aqueous solution, but is largely and quickly

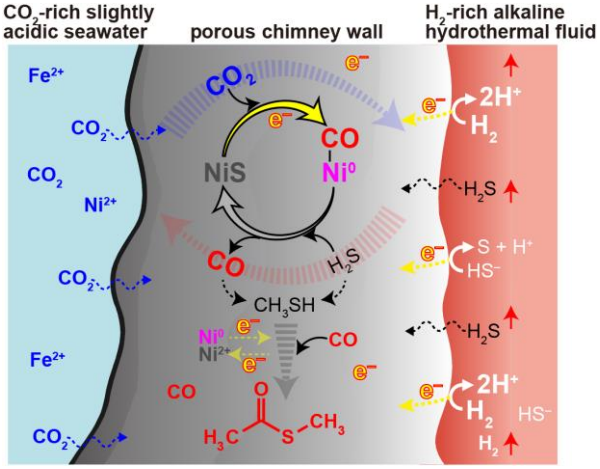

Fig. 3. Schematic cross-section of a vent chimney in an early ocean alkaline hydrothermal system showing possible abiotic thioester synthesis promoted by Ni sulfide_PERM.

released in the presence of adsorption competitors such as methanethiol and hydrogen sulfide (see supplementary text, figs. S28 and S29). Thus, considering dynamic mixing of hydrothermal fluids with seawater observed in the present-day deep-sea vent chimneys through the pore systems (*23*), continuous CO production, concentration, desorption, and advection are likely to have occurred within the pore spaces of ancient hydrothermal mineral deposits (Fig. 3). Such fluid-mediated materials transport favors the occurrence and combination of multiple reactions including the formation of thiols from CO (or CO_2) and H_2S (*24*,*25*), the condensation of CO with methanethiol to form MTA (Fig. 2B to D), and the accumulation of organic products (*26*). Thus, the thioester synthesis via the formation of Ni sulfide_PERMs should have been robustly concomitant with ubiquitous hydrothermal activities on the primordial seafloor.

Nowadays, growing consensus for CO_2 as the dominant carbon species on the Hadean Earth has stimulated exploration of geo- and astro-chemical events that could have transiently realized highly reducing early atmosphere (*27*). Subsequent photochemical and aqueous-phase processes with reactive carbon sources, powerful oxidizing/reducing agents, and/or UV light might have realized abiotic thioester synthesis (*28*,*29*). Although these reactions might have played a role in enrichment of a prebiotic soup, their relevance to biosynthesis is ambiguous. Consequently, numerous questions remain unanswered by the transient scenario regarding the gap between prebiotic chemistry and early biochemistry conserved in the metabolic and phylogenetic architectures of life.

The two key observations, our experimental results demonstrating the CO_2 fixation capability of Ni sulfide_PERMs (Fig. 2) and the central role of Ni at the active sites of CODH/ACS (*5*), may lead to a plausible scenario for the emergence of protometabolism prior to the origin of life. Sustained occurrence of electrochemical energy adequate for the Ni sulfide_PERM formation, $\leq$–0.6 V_{SHE} in the ancient seawater condition (Figs. 1 and 2), is limited in nature except for deep-sea hydrothermal settings (fig. S1). This environmental specificity with the known necessity of Ni in both biological and chemical CO_2 fixation suggest that the Ni sulfide_PERM-promoted thioester synthesis in early ocean hydrothermal systems (Fig. 3) is a primordial precursor of the CODH/ACS reaction. The CO production on metal-sulfide_PERMs (Fig. 2A) may also have served as crucial carbon and energy sources for the early chemolithotrophic ecosystem, thereby supporting, or even directing, the origin and early evolution of autotrophs as suggested from the autotrophic metabolism core (*30*).

References and Notes

1. P. S. Adam, G. Borrel, S. Gribaldo, Evolutionary history of carbon monoxide dehydrogenase/acetyl-CoA synthase, one of the oldest enzymatic complexes. *Proc. Natl. Acad. Sci. USA* **115**, E1166–E1173 (2018).
2. M. J. Russell, W. Martin, The rocky roots of the acetyl-CoA pathway, *TRENDS Biochem. Sci.* **29**, 358–363 (2004).
3. F. L. Sousa, T. Thiergart, G. Landan, S. Nelson-Sathi, I. A. C. Pereira, J. F. Allen, N. Lane, W. F. Martin, Early bioenegetic evolution. *Phil. Trans. R. Soc. B.* **368**, 20130088 (2013).
4. K. Schuchmann, V. Müller, Autotrophy at the thermodynamic limit of life: a model for energy conservation in acetogenic bacteria. *Nature Rev. Microbiol.* **12**, 809–821 (2014).
5. M. Can, L. J. Giles, S. W. Ragsdale, R. Sarangi, X-ray absorption spectroscopy reveals an organometallic Ni–C bond in the CO-treated form of acetyl-CoA synthase, *Biochem.* **56**, 1248–1260 (2017).
6. C. Huber, G. Wächtershäuser, Activated acetic acid by carbon fixation on (Fe,Ni)S under primordial conditions. *Science* **276**, 245–247 (1997).
7. M. Yamamoto, R. Nakamura, T. Kasaya, H. Kumagai, K. Suzuki, K. Takai, Spontaneous and widespread electricity generation in natural deep-sea hydrothermal fields. *Angew. Chem. Int. Ed.* **56**, 5725–5728 (2017).
8. R. Ang, A. U. Khan, N. Tsujii, K. Takai, R. Nakamura, T. Mori, Thermoelectricity generation and electron–magnon scattering in a natural chalcopyrite mineral from a deep-sea hydrothermal vent. *Angew. Chem. Int. Ed.* **54**, 12909–12913 (2015).
9. J. Krissansen-Totton, G. N. Arney, D. C. Catling, Constraining the climate and ocean pH of the early Earth with a geological carbon cycle model. *Proc. Natl. Acad. Sci. USA* **115**, 4105–4110 (2018).
10. A. Yamaguchi, M. Yamamoto, K. Takai, T. Ishii, K. Hashimoto, R. Nakamura, Electrochemical CO_2 reduction by Ni-containing iron sulfides: How is CO_2 electrochemically reduced at bisulfide-bearing deep-sea hydrothermal precipitates? *Electrochim. Acta* **141**, 311–318 (2014).
11. H. Ooka, S. E. McGlynn, R. Nakamura, Electrochemistry at deep-sea hydrothermal vents: utilization of the thermodynamic driving force towards the autotrophic origin of life. *ChemElectroChem* **6**, 1316–1323 (2019).
12. N. Kitadai, R. Nakamura, M. Yamamoto, K. Takai, Y. Li, A. Yamaguchi, A. Gilbert, Y. Ueno, N. Yoshida, Y. Oono, Geoelectrochemical CO production: Implications of the autotrophic origin of life. *Sci. Adv.* **4**, eeao7265 (2018).

13. N. Kitadai, R. Nakamura, M. Yamamoto, K. Takai, Y. Oono, Metals likely promoted protometabolism in early ocean alkaline hydrothermal systems. *Sci. Adv.* **5**, eeav7848 (2019).
14. W. Zhu, X. Yue, W. Zhuang, S. Yu, Y. Zhuang, J. Wang, J. Wang, Nickel sulfide microsphere film on Ni foam as an efficient bifunctional electrocatalyst for overall water splitting. *Chem. Commun.* **52**, 1486–1489 (2016).
15. H. Xiao, W. A. Goddard III, T. Cheng, Y. Liu, Cu metal embedded in oxidized matrix catalyst to promote CO_2 activation and CO dimerization for electrochemical reduction of CO_2. *Proc. Natl. Acad. Sci.* 114, 6685–6688 (2017).
16. Y. Hori, A. Murata, Electrochemical evidence of intermediate formation of adsorbed CO in cathodic reduction of CO_2 at a nickel electrode. *Electrochim. Acta* **35**, 1777–1780 (1990).
17. H. A. Hansen, J. B. Varley, A. A. Peterson, J. K. Norskov, Understanding trends in the electrocatalytic activity of metals and enzymes for CO_2 reduction to CO. *J. Phys. Chem. Lett.* **4**, 388–392 (2013).
18. V. Hirschbeck, P. H. Gehrtz, I. Fleisher, Metal-catalyzed synthesis and use of thioesters: recent developments. *Chem. Eur. J.* **24**, 7092–7107 (2018).
19. W. Erley, H. Wagner, Sulfur poisoning of carbon monoxide adsorption on Ni(111). *J. Catal.* **53**, 287–294 (1978).
20. S. H. Ma, Z. Y. Jiao, T. X. Wang, X. T. Zu, Effect of preadsorbed S on the adsorption of CO on Co(0001). *J. Phys. Chem.* **113**, 16210–16215 (2009).
21. A. Bekker, M. E. Barley, M. L. Fiorentini, O. J. Rouxel, D. Rumble, S. W. Beresford, Atmospheric sulfur in Archean komatiite-hosted nickel deposits. *Science* **326**, 1086–1089 (2009).
22. P. L. Morrill, J. G. Kuenen, O. J. Johnson, S. Suzuki, A. Rietze A. L. Sessions, M. L. Fogel, K. H. Nealson, Geochemistry and geobiology of a present-day serpentinization site in California: The Cedars. *Geochim. Cosmochim. Acta* **109**, 222–240 (2013).
23. M. K. Tivey, Generation of seafloor hydrothermal vent fluids and associated mineral deposites. *Oceanography* **20**, 50–65 (2007).
24. W. Heinen, A. M. Lauwers, Organic sulfur compounds resulting from the interaction of iron sulfide, hydrogen sulfide and carbon dioxide in an anaerobic aqueous environment. *Orig. Life Evol. Biosph.* **26**, 131–150 (1996).
25. M. D. Schulte, K. L. Rogers, Thiols in hydrothermal solution: standard partial molal properties and their role in the organic geochemistry of hydrothermal environments. *Geochim. Cosmochim. Acta* **68**, 1087–1097 (2004).
26. P. Baaske, F. M. Weinert, S. Duhr, K. H. Lemke, M. J. Russell, D. Braun, Extreme accumulation of nucleotides in simulated hydrothermal pore systems. *Proc. Natl. Acad. Sci.* **104**, 9346–9351 (2007).
27. S. A. Benner, E. A. Bell, E. Biondi, R. Brasser, T. Carell, H. J. Kim, S. J. Mojzsis, A. Omran, M. A. Pasek, D. Trail, When did life likely emerge on Earth in an RNA-first process? *ChemSystemsChem* **1**, e1900035 (2019).
28. A. L. Weber, Nonenzymatic formation of "energy-rich" lactoyl and glyceroyl thioesters from glyceraldehyde and a thiol. *J. Mol. Evol.* **20**, 157–166 (1984).
29. E. Chevallot-Beroux, J. Gorges, J. Moran, Energy conservation via thioesters in a non-enzymatic metabolism-like reaction network. *ChemRxiv* (2019) DOI:10.26434/chemrxiv.8832425.
30. S. W. Ragsdale, Life with carbon monoxide, *Crit. Rev. Biochem. Mol. Biol.* **39**, 165–195 (2004).
31. M. Aono, N. Kitadai, Y. Oono, A principled approach to the origin problem. *Orig. Life. Evol. Biopsh.* **45**, 327–338 (2015).

Acknowledgments: We thank Reiko Nagano and Atsuko Fujishima for their help in laboratory experiments. **Funding:** This research was supported by JSPS KAKENHI (Grant Number; 18H04456) and the Astrobiology Center Program of NINS (Grant Number; AB292004). **Author contributions:** N.K and Y.O. conceived the whole project based on the principled approach (*31*) and N.K. realized nonenzymatic thioester synthesis. Y.T. measured XANES spectra of the sulfide samples. S.O. performed SEM-EDX analysis, and W.T. prepared figures for the SEM-EDX data. N.K. performed all experiments except for the XANES and SEM-EDX measurements with technical support of Y.N., and prepared all figures and tables for the obtained results. All authors contributed to writing the paper. **Competing interests:** Authors declare no competing interests. **Data and materials availability:** All data is available in the main text or the supplementary materials.

Materials and Methods

Preparation of metal sulfides

All metal sulfides were prepared by adding 100 mM sodium sulfide (Na_2S) dropwisely into the corresponding 100 mM metal chlorides ($NiCl_2$, $FeCl_2$, or $CoCl_2$) or their binary mixtures (for example, 50 mM $NiCl_2$ plus 50 mM $FeCl_2$) under vigorous stirring to a final volume ratio of 1:1. Solid precipitates were then separated from the supernatant solutions by centrifugation (8000 rpm, 10 min) and were dried under vacuum. To prevent oxidation by atmospheric O_2, the sample preparation was conducted in a glove box filled with N_2 gas (>99.99995%), with 4% H_2 being added (the COY system). All chemicals were purchased from

FUJIFILM Wako Pure Chemical Corporation as reagent grade. Deaerated Milli-Q water (18.2 megohms) was used as the solvent.

Pure metals (Fe^0, Co^0, and Ni^0) were obtained from EM Japan. Their reported characteristics and XRD patterns measured in the present study are presented in Table S1 and fig. S9, respectively.

Sulfide electrolysis

Metal sulfide electrolysis was conducted under a simulated early ocean condition in accordance with the procedure reported previously (*13*). Briefly, 400 mg of sulfide samples was deposited on a carbon working electrode (5.7 cm^2) in a H-type cell (fig. S2), immersed in a deaerated 100 mM NaCl, and exposed to a flow (20 ml min^{-1}) of CO_2 (>99.995%) containing 4 ppm of H_2S. The CO_2 gas buffered the solution pH at slightly acidic (6.0 ± 0.25). The H_2S partial pressure was determined by thermodynamic calculation to supply H_2S and HS^- into solution with the equilibrium total concentration of 0.5 μmol kg^{-1}. Although the ionic strength and pressure conditions adopted in this experiment are different from the ancient deep-sea hydrothermal settings (*32*,*33*), a thermodynamic calculation indicates that these differences have no significant influence on the redox potentials for the sulfide/metal and the CO_2/CO systems (fig. S5) (*13*).

While keeping the CO_2 gas flow that was started at least 1 hour before each experiment, a constant potential was applied on the carbon electrode for 7 days by using a multi-potentiostat (PS-08; Toho Technical Research). All potentials were measured against an Ag/AgCl reference electrode in saturated KCl and were converted to the SHE scale by the following equation

$$E\ (\text{versus SHE}) = E\ (\text{versus Ag/AgCl}) + 0.198\ \text{V} \qquad (1)$$

After the electrolysis, the electrochemical cell was immediately transferred into a glove box filled with N_2 and H_2 gases (volume ratio, 96:4). The solid sample was then separated from the supernatant solution, dried under vacuum for 1 hour, and stored inside the glove box. A dry vacuum pump (RDA-281H, ULVAC) with the reported ultimate pressure of 0.08 Pa was used for the dehydration. The surface-bound CO on zerovalent metal sites was expected to be intact at this vacuum condition (*19, 34, 35*).

Solid characterization

Scanning electron microscopy (SEM) imaging was performed on a Helios G4 UX equipped with a Quorum PP-3010 cryo preparation system and an AMTEC Octane Super C5 EDS detector. An acceleration voltage of 2 kV was applied for secondary electron imaging and 20 kV for energy dispersive X-ray spectroscopy (EDS) analysis under a reduced pressure of < 1×10^{-4} Pa at room temperature (23 ± 2°C). Samples were prepared as follows. First, sulfide sample sealed in a serum bottle was placed in a vacuum chamber of the cryo-preparation system, whose internal atmosphere was replaced with N_2 gas from liquid N_2 vaporization by three times of evacuation-purge cycles. Under flow of N_2 gas, the serum bottle was opened, and the sulfide was rubbed onto a carbon tape (Nisshin EM) attached on a transfer shuttle by a plastic spatula. The shuttle was transferred into a transfer device under ~10^2 Pa, and then to the SEM chamber via a cryo-preparation chamber (<10^{-4} Pa).

Particle size distribution (fig. S6) was determined by manual segmentation on Affinity Photo for iPad 1.6.8.77 (Serif (Europe) Ltd.) followed by image analysis with Image-Pro 3D v9.3 (Media Cybernetics). Particle diameters were calculated from the segmented areas assuming spherical morphology.

X-ray diffraction (XRD) patterns of sulfide samples were measured by using an X-ray diffractometer with Cu Kα radiation (MiniFlex 600, Rigak). All runs were conducted with 2θ ranging from 10° to 90° using 0.02° 2θ step with a scan rate of 0.1 or 1° min^{-1}. To prevent oxidation by atmospheric O_2 during the measurement, the solid samples were shielded in an air-sensitive sample holder (Rigaku). Peak identifications were made on the basis of the reference patterns reported in the Powder Diffraction File published by the International Centre for Diffraction Data. The reference patterns are presented in Fig. 1A, figs. S8 to S11 with the measured XRD data.

X-ray absorption near-edge structure (XANES) spectra at Ni and Co K-edges were measured at BL-12C (bending magnet beamline) in a synchrotron radiation facility (Photon Factory) in High Energy Accelerator Research Organization (KEK), Tsukuba, Japan. In the beamline, X-ray from a synchrotron operated at 2.5 GeV (current: 450 mA) was monochromatized with a Si(111) double-crystal monochromator, and focused to an area of 0.5 × 0.5 mm^2 with a bent cylindrical mirror, which also reduced the higher order. XANES spectra were obtained in transmission mode using two ion chambers to measure intensities of incident (I_0) and transmitted (I) X-rays. Energy step within the XANES region was 0.25 eV, and the absorbance by the sample (μt) was obtained as $\mu t = \ln(I/I_0)$. Sulfide samples were diluted with boron nitride (BN, <150 nm, 99% purity) to yield the metal/BN molar ratio of 1:25, and shielded **by** an O_2-impermeable polyethylene film. Measurement was conducted for a part of the sample with uniform thickness within the area of the X-ray beam.

Quantification of the surface-bound CO on electrolyzed sulfides

Each sulfide sample (50 mg for each) was sealed in a serum bottle (124.7 ml) with a Teflon-laminated butyl rubber cap and an aluminum stopper in a glove box filled with N_2 and H_2 gases (volume ratio, 96:4). The bottle was then filled with pure He gas (>99.99995%) by flowing the He through a stainless needle at a rate of 100 ml min^{-1} over 10 min. This was followed by the addition of 5 ml of 35% HCl (super special grade; FUJIFILM) under vigorous agitation. After the sulfide sample dissolved completely under 60 rpm min^{-1} rotation of the bottle at room temperature (25 ± 2°C) (typically, within 30 min), the headspace gas was analyzed by gas chromatography (GC) (Fig. 2A, fig. S18, and Table S2). No CO was detected in a blank experiment in the absence of sulfide.

Movie S1 presents a demonstration of the surface-bound CO on the NiS electrolyzed at –1.0 V_{SHE}. A weak acid (1 M H_3PO_4) was used here to make clear the gas bubble formation from the electrolyzed surface by reducing NiS dissolution.

To ensure reproducibility, we carried out multiple independent runs using several sulfide samples for each metal. Differences among the data obtained at the identical condition were less than 20%. The same was true for the following two experiments.

Nonenzymatic thioester synthesis

Each sulfide sample (50 mg for each) was sealed in a serum bottle (13.8 ml) with a Teflon-laminated butyl rubber cap and an aluminum stopper in a glove box filled with N_2 and H_2 gases (volume ratio, 96:4). The bottle was then filled with pure CO_2 gas (>99.995%) by flowing the CO_2 through a stainless needle at a rate of 100 ml min^{-1} over 5 min. This was followed by the addition of 0.75 ml of 100 mM sodium methathiolate (CH_3SNa) with or without 1.86 ml of CO gas (1 atm, 99.9% purity). After rotating the bottle at 60 rpm min^{-1} for 7 days at room temperature (25 ± 2°C), the headspace gas was analyzed by GC (Fig. 2B to D, figs. S19 to S23, and Tables S3 and S4). The aqueous suspension was then centrifuged (10000 rpm, 2 min) and measured for pH by a portable pH meter (Seven2Go Pro, Mettler Toledo).

The MTA synthesis was also examined under various experimental conditions. See Supplementary Text for details and obtained results. All data support our discussion on the reaction mechanism described in the main text.

Competitive adsorption of CO with H_2S

Sulfide sample (50 mg for each) was sealed in a serum bottle (19.5 ml) with a Teflon-laminated butyl rubber cap and an aluminum stopper in a globe box filled with N_2 and H_2 gases (volume ratio, 96:4). The bottle was then filled with pure He gas (>99.99995%) by flowing the He through a stainless needle at a rate of 100 ml min^{-1} over 5 min. This was followed by the addition of 1 ml of 300 mM Na_2S and the subsequent addition of 1 ml of 450 mM HCl. After rotating the bottle at 60 rpm min^{-1} for one day at room temperature (25 ± 2°C), the headspace gas was analyzed by GC (figs. S28 and S29 and Table S5). No carbon-sulfur compounds (for example, methanethiol, carbon disulfide, carbonyl sulfide) were detected.

From the pH values of aqueous suspensions (7.5–8.0; Table S5), the initial dissolved H_2S and HS^- concentrations are predicted to be 90–120 mM in total assuming equilibrium H_2S distribution in the gas and liquid phases without the surface adsorption.

Sample analysis

Inorganic gases including H_2, CO, and CH_4 were quantified by a Shimadzu GC system equipped with a BID-2010 Plus detector (Tracera). A MICROPACKED-ST column (Shinwa) was attached. He (>99.99995%) was used as the carrier gas at a column flow rate of 7 ml min^{-1}. The column temperature was initially kept at 35°C for 2.5 min, raised to 250°C at a rate of 20°C min^{-1}, and then raised to 265°C at a rate of 4°C min^{-1}. A chromatogram for a standard gas sample is shown in fig. S14 with obtained calibration curves.

Gas-phase sulfur compounds were analyzed using a Shimadzu gas chromatogram-mass spectrometer (GCMS-QP2010 Ultra) equipped with a DB–SULFUR SCD column (60 m, 0.32 mm I.D, Agilent). He (>99.99995%) was used as the carrier gas at a column flow rate of 33.2 cm sec^{-1}. The column temperature was initially kept at 35°C for 5 min, raised to 155°C at a rate of 10°C min^{-1}, and then raised to 235°C at a rate of 20°C min^{-1}. The scan range was set to m/z 5–200 Da. Compounds were identified from comparisons of retention time and mass spectrum with standards prepared from commercial reagents, and quantified based on calibration curves (fig. S15). Several gas samples were also analyzed by the Tracera GC system with a DB–SULFUR SCD column at the measurement condition described in this paragraph (fig. S16).

Aqueous-phase products were characterized, after filtration with a polytetrafluoroethylene membrane filter (pore size, 0.2 μm), by using a Shimadzu HPLC system equipped with an electric conductivity detector and an anion exchange column (Shim-pack SCR-102H, Shimadzu) set at 40°C. The p-toluenesulfonic acid aqueous solution (5 mM) was used as the eluent at a rate of 1.6 ml min^{-1}. A chromatogram for several organic acids is shown in fig. S17 with the obtained calibration curves.

Thermodynamic calculation

Redox potentials (E_h) of the H^+/H_2 and the CO_2/CO couples as functions of temperature and pH (fig. S1) were calculated with the following equations

$$E_h = \frac{1}{2F}\left(2RT\ln\alpha_{H^+} - RT\alpha_{H_2} - \Delta_f G^o(H_2)\right) \quad (1)$$

$$E_h = \frac{1}{2F}\begin{pmatrix} 2RT\ln\alpha_{H^+} + RT\ln\alpha_{CO_2} - RT\ln\alpha_{CO} \\ +\Delta_f G^o(CO_2) - \Delta_f G^o(CO) - \Delta_f G^o(H_2O)\end{pmatrix} \quad (2)$$

In these equations, T, R, and F stand for temperature in kelvins, the gas constant (8.31447 J mol^{-1} K^{-1}), and the Faraday constant (96485 J mol^{-1} V^{-1}), respectively. α_i represents the activity of the species i that was calculated either using the extended Debye-Hückel equation (*36*) for aqueous ionic species (H^+) or setting the activity coefficient to unity for aqueous neutral species (H_2, CO_2 and CO). $\Delta_f G^o$(i) signifies the standard Gibbs energy of formation of the species i at the temperature and pressure of interest, which were calculated according to the revised HKF equations of state (*37*) together with the thermodynamic data and the revised HKF parameters reported in (*38*) for H_2 and CO_2 and in (*39*) for CO. $\Delta_f G^o$ of H_2O was taken from Helgeson and Kirkham *(40)*.

In fig. S1, 1 mmol kg^{-1} H_2 was considered because it is a typical H_2 concentration in fluids from the present-day serpentine-hosted hydrothermal systems (*23*, *41*). The CO_2/CO activity ratio was set to one. Equilibrium calculation with this ratio gives the potential conditions where CO_2 and CO are equally stable. A ten-fold change in the activity ratio changes the redox potential by ± ~30 mV at 25°C and by ± ~40 mV at 150°C.

The potential/pH diagrams of the sulfide–metal systems (Fig. 1B and fig. S4) were computed with the Act2 program in Geochemist's Workbench version 10.0.5 by using the thermodynamic dataset for aqueous species calculated by the above procedures, those for sulfide minerals listed in table S3 presented by Kitadai et al. (*13*), and those for pure metals compiled in Robie and Hemingway (*42*).

Supplementary Text

Quantification of the surface-bound CO on electrolyzed sulfides

To verify the CO production and accumulation on the electrolyzed NiS, we conducted the following experiment with isotopically labeled sodium bicarbonate ($NaH^{13}CO_3$, 99% purity) provided by Cambridge Isotope Laboratories, Inc.. First, 400 mg of NiS was electrolyzed at –1.0 V_{SHE} for 7 days in 60 ml of 0.5 M phosphate buffer solution (pH 6.0) under pure N_2 gas flow (>99.9998%). Then, the gas headspace of the electrochemical cell (~40 ml) was purged with $^{13}CO_2$ gas that was provided by a dropwise addition of 0.1 M phosphoric acid (H_3PO_4) onto $NaH^{13}CO_3$ powder under vigorous stirring in a closed vial connected with the electrochemical cell with a polyvinyl chloride tube and stainless needles. After additional two hour electrolysis with the gas inlet and outlet closed, the NiS on the carbon paper was collected, dried under vacuum, and dissolved completely in 35% HCl (see Materials and Methods). GC-MS analysis of the released gas revealed the formation of ^{13}CO with the m/z = 29 (fig. S18C). No ^{13}CO was detected in the $^{13}CO_2$ formed by the H_3PO_4 addition to $NaH^{13}CO_3$ (fig. S18C).

In the normal CO_2 gas bubbled during the electrolysis of sulfide samples, we detected no CO with our GC's maximum performance (detection limit; ~1 ppm). Even if a very slight amount of CO impurity is present in the CO_2, its contribution to the surface-bound CO (Fig. 2A and Table S2) must be negligible because the electrolyzed FeS released almost no CO despite the fact that Fe^0 has an even stronger CO binding energy than Ni^0 and CO^0 (*43*).

Nonenzymatic thioester synthesis

The four organosulfur compounds observed in the present study (methanethiol, MTA, dimethyl sulfide, and dimethyl disulfide) distribute both the gas- and aqueous-phases with significant fractions. Thus, aqueous-phase concentrations of methanethiol, dimethyl sulfide, and dimethyl disulfide were calculated from the partial pressures of respective compounds quantified by GC with the Henry's law constants reported in the literature (0.38, 0.56, and 0.58 mol l^{-1} atm^{-1}, respectively) (*44*). The constant for MTA was determined experimentally to be 5.8 ± 1.0 mol l^{-1} atm^{-1} from three independent measurements of the water-gas partitioning of MTA in a closed glass vial containing a certain volume of 100 mM phosphate buffer solution (pH 6.7). The constants for methanethiol, dimethyl sulfide, and dimethyl disulfide determined by this method were in agreement with the literature values with the percentage errors less than 15%.

The organosulfur compounds may also be present on the sulfide surfaces. Actually, when 1 M phosphoric acid (H_3PO_4) was added after the 7-day interaction of methanethiol with the NiS electrolyzed at –1.0 V_{SHE}, the gas-phase MTA and methanethiol concentrations increased by 30 and 70%, respectively, while that of dimethyl sulfide decreased by 50%. Nevertheless, because such chemical processes may cause undesirable reactions that consume MTA, we did not take account of the surface adsorption in the yield determination of organosulfur compounds. For the same reason, in this experiment, we report the amounts of inorganic gases (H_2, CO, and CH_4) quantified from the gas-phase analysis alone (figs. S19B and S22 and S23, Table S3 and S4).

Dimethyl disulfide was always observed in the presence of methanethiol with the amount typically less than a few percent of the initial amount of methanethiol (figs. S19A and

S20). A probable cause of the dimethyl disulfide formation is methanethiol oxidation by atmospheric O_2 ($2\ CH_3SH + 0.5\ O_2 \rightarrow CH_3SSCH_3 + H_2O$) at the timing of sample injections into the GC system owing to air intrusion (fig. S19B). Except for dimethyl disulfide, no oxidative organosulfur compound was detected (fig. S20). It was also confirmed that MTA, dimethyl sulfide, and dimethyl disulfide were stable in air.

With the NiS_PERM prepared at –1.0 V_{SHE}, we observed the following product characteristics. The yield of MTA increased over one week, while the amounts of CO and methanethiol decreased from their maxima at the beginning (fig. S24). CO appeared in the gas-phase through competitive adsorption with methanethiol; in the absence of methanethiol under otherwise identical condition, few CO gas was detected (0.03 μmol) and no MTA was observed (fig. S21A). As long as methanethiol was available, the initial compositions of gas-phase and aqueous electrolyte had no significant influence on the MTA formation. Replacement of CO_2 with helium (He), and dissolution of 1 M phosphate (pH 7.0) into the sample solution resulted in the MTA yield of 3.6 ± 0.7 μmol after the 7-days reaction, which is almost equal to the original value (3.2 ± 0.6 μmol; Fig. 2B). It was also confirmed using ^{13}C-labeled CO_2 that the CO_2 filled in the serum bottle did not serve as a carbon source of MTA. The MTA formed under $^{13}CO_2$ atmosphere showed the identical mass spectrum to that of the standard MTA with normal carbon isotopic composition.

In aqueous solutions, acetate (0.19 ± 0.04 μmol or 0.25 ± 0.05 mM) and formate (0.03 ± 0.01 μmol or 0.035 ± 0.01 mM) were observed (fig. S25). The acetate concentration increased to 2.0 ± 0.4 mM when the product solution was basified by 1 M sodium hydroxide (NaOH) due to MTA hydrolysis. Because MTA hydrolysis is accelerated at elevated temperatures (*45*), one-day experiments at 80°C resulted in higher yield of acetate (2.4 ± 0.5 μmol or 3.2 ± 0.6 mM) and lower yield of MTA (0.68 ± 0.14 μmol) (Fig. S25). Other biologically relevant organic acids such as pyruvate and lactate were not detected in any product solutions with concentrations higher than 0.01 mM. We also treated solid samples with 8 M potassium hydroxide (KOH) after the reaction, but neither pyruvate nor lactate was observed.

Basified aqueous samples stored in non-airtight containers over several days occasionally showed 1–10 μM of acetate and pyruvate signals (data not shown), because basification facilitates absorption of organic acids from ambient air. Thus, especially to avoid crucial contaminations such as pyruvate we set our detection cutoff at 0.01 mM and analyzed all aqueous samples as soon as they were prepared.

Figure S27 depicts possible intermediate steps for the dimethyl sulfide and CH_4 formations on NiS_PERM. Because their yields decreased steeply when the NiS electroreduction potential was positively changed from –1.0 to –0.8 V_{SHE} (figs. S22 and S23) as was the case with MTA, closely distributed multiple surface Ni^0 sites are expected to be also advantageous to these formations.

References

32. J. P. Amend, T. M. McCollom, Energetics of biomolecule synthesis on early Earth, in *Chemical Evolution II: From the Origins of Life to Modern Society*, L. Zaikowski, J. M. Fredrich, S. R. Seidel, Eds. (American Chemical Society, 2009), pp. 63–94.
33. T. Shibuya, M. J. Russell, K. Takai, Free energy distribution and hydrothermal mineral precipitation in Hadean submarine alkaline vent systems: Importance of iron redox reactions under anoxic conditions. *Geochim. Cosmochim. Acta* **175**, 1–19 (2016).
34. M. E. Bridge, C. M. Comrie, R. M. Lambert, Chemisorption studies on cobalt single crystal surfaces I. carbon monoxide on Co(0001). *Surf. Sci.* **67**, 393–404 (1977).
35. L. Gonzalez, R. Miranda, S. Ferrer, A thermal desorption study of the adsorption of CO on Fe(110); enhancement of dissociation by surface defects. *Sur. Sci.* **119**, 61–70 (1982).
36. H. C. Helgeson, D. H. Kirkham, G. C. Flowers, Theoretical prediction of the thermodynamic behavior of aqueous electrolytes at high pressures and temperatures: IV. Calculation of activity coefficients, osmotic coefficients, and apparent molal and standard and relative partial molal properties to 600°C and 5 KB. *Am. J. Sci.* **281**, 1249–1516 (1981).
37. E. L. Shock, E. H. Oelkers, J. W. Johnson, D. A. Sverjensky, H. C. Helgeson, Calculation of the thermodynamic properties of aqueous species at high pressures and temperatures. *J. Chem. Soc. Faraday Trans.* **88**, 803–826 (1992).
38. E. L. Shock, H. C. Helgeson, D. A. Sverjensky, Calculation of the thermodynamic and transport properties of aqueous species at high pressures and temperatures: Standard partial molal properties of inorganic neutral species. *Geochim. Cosmochim. Acta* **53**, 2157–2183 (1989).
39. E. L. Shock, W. B. McKinnon, Hydrothermal processing of cometary volatiles–applications to triton. *Icarus* **106**, 464–477 (1993).
40. H. C. Helgeson, D. H. Kirkham, Theoretical prediction of the thermodynamic behavior of aqueous electrolytes at high pressures and temperatures: I. summary of the thermodynamic/electrostatic properties of the solvent. *Am. J. Sci.* **274**, 1089–1198 (1974).

41. M. O. Schrenk, W. J. Brazelton, S. Q. Lang, Serpentinization, carbon, and deep life. *Rev. Mineral. Geochem.* **75**, 575–606 (2013).
42. R. A. Robie, B. S. Hemingway, "*Thermodynamic Properties Of Minerals And Related Substances At 298.15 K And 1 Bar (10^5 Pasals) Pressure And At Higher Temperatures*" (U.S. Geological Survey Bulletin 2131, U.S. Geological Survey, 1995).
43. F. Abild-Pedersen, M. P. Andersson, CO adsorption energies on metals with correction for high coordination adsorption sites – A density functional study. *Surf. Sci.* **601**, 1747–1753 (2007).
44. R. Sander, Compilation of Henry's law constants (version 4.0) for water as solvent. *Atmos. Chem. Phys.* **15**, 4399–4981 (2015).
45. K. Chandru, A. Gillbert, C. Butch, M. Aono, H. J. Cleaves II, The abiotic chemistry of thiolated acetate derivatives and the origin of life. *Sci. Rep.* **6**, 29883 (2016).
46. L. L. Van Loon, C. Throssell, M. D. Dutton, Comparison of nickel speciation in workplace aerosol samples using sequential extraction analysis and X-ray absorption near-edge structure spectroscopy. *Environ. Sci. Processes Impacts* **17**, 922–931 (2015).
47. M. E. Fleet, The crystal structure of heazlewoodite, and metallic bonds in sulfide minerals. *Am. Mineral.* **62**, 341–345 (1977).
48. M. Can, F. A. Armstrong, S. W. Ragsdale, Structure, function, and mechanism of the nickel metalloenzymes, CO dehydrogenase, and acetyl-CoA synthase. *Chem. Rev.* **114**, 4149–4174 (2014).